ARTICLE

Chinese Journal of Structural Chemistry

Co-Construction of Sulfur Vacancies and Heterogeneous Interface into Ni_3S_2/MoS_2 Catalysts to Achieve Highly Efficient Overall Water Splitting

Zhaoyang An[1], Hui Xue[1]*, Jing Sun[1], Niankun Guo[1], Tianshan Song[1], Jiawen Sun[1], Yi-Ru Hao[1] and Qin Wang[1]*

[1]*College of Chemistry and Chemical Engineering, Inner Mongolia University, Hohhot 010021, China*

ABSTRACT Integrating the advantages of anion vacancies and heterostructures into the catalytic materials may increase the binding affinities to intermediates, provide more active sites, and significantly promote the activity of overall water splitting. However, the successful assembly of anion vacancies and heterostructures for high-efficiency water splitting performance is still challenging. In this work, we ingeniously present the co-construction of sulfur vacancies and heterogeneous interface into Ni_3S_2/MoS_2 catalysts on nickel foam (NF). The introduction of sulfur vacancies and Ni_3S_2/MoS_2 heterostructures can significantly improve electron and ion transport, effectively improve structural stability, and enhance overall water splitting activity. The obtained V_S-Ni_3S_2/MoS_2 catalysts (V_S stands for sulfur vacancies) exhibit superior OER and HER activities, and the overpotentials for OER and HER are 180 and 71 mV at 10 mA·cm^{-2}, respectively. Furthermore, a low water splitting voltage of 1.46 V is required at 10 mA·cm^{-2} for the V_S-Ni_3S_2/MoS_2 catalysts, which is considerably lower than most that of water splitting electrocatalysts currently reported. This work offers an effective mean for the preparation of catalysts with both anion vacancies and heterostructures for achieving high-performance alkaline overall water splitting.

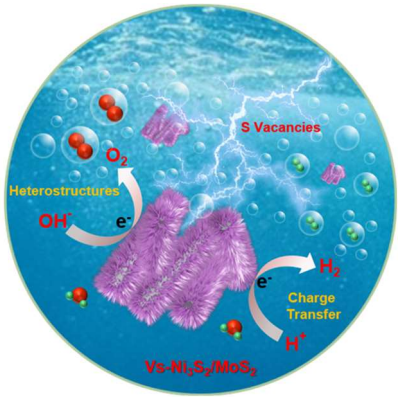

Keywords: sulfur vacancies, heterostructures, transition metal chalcogenides, overall water splitting

INTRODUCTION

In today's era of energy scarcity, many favorable strategies, including photochemical, photoelectrochemical, and electrochemical water splitting have been used to achieve sustainable H_2 production.[1-4] Nevertheless, the large overpotentials of oxygen evolution reaction (OER) and hydrogen evolution reaction (HER) during the process of water splitting need to be overcome by efficient catalysts. At present, the commercial Pt/C with near-zero overpotential is regarded as the most effective HER electrocatalyst, and so is RuO_2 for OER electrocatalyst.[5] However, it is unrealistic for these noble-metal-based electrocatalysts used as commercial electrolyzers on a large scale due to the high-cost and rareness.[6] There are a large number of intermediates on the superficies of the catalysts, such as H^+, OOH*, and OH*, and the chemisorption and dissociation of the intermediates determine the water-oxidation activity for the alkaline OER. Hence, the combination of oxygen- and hydrogen-containing intermediates is conducive to the construction of OER electrocatalysts with advantages of water oxidation.[7] On the other hand, a delicate balance between the activity of water splitting (the Volmer step) and the chemisorption of intermediates (OH^- and H*) determines the kinetics of HER in alkaline solution. Thus, synthesis of catalysts that can promote the interactive chemisorption of both H^* and OH^- intermediates on the surface is beneficial to improve the HER activity.[8] Therefore, chemisorption free energy of hydrogen- or oxygen-containing intermediates is a significant foundation to construct the OER, HER, and overall water splitting electrocatalysts.[9-12]

Molybdenum-based nanomaterials, particularly MoS_2, have been widely researched as the HER electrocatalysts.[13] Because the unsaturated Mo-S sites along the MoS_2 boundary possess high chemisorption capacity for hydrogen, MoS_2 shows HER activity similar to that of precious metal Pt, which can be confirmed by both DFT calculations and experimental studies.[14] In addition, extensive transition metal such as Fe, Co, and Ni have been developed for OER electrocatalysts, especially their oxides,[15] hydroxides,[16] layered double hydroxides (LDHs),[17] and sulfides.[18] At present, transition metal chalcogenides with the superiority of environmental friendliness, unique electronic structure and excellent electrocatalytic performance have been regarded as the effective OER catalysts. The undercoordinated metal sites on the superficies of transition metal chalcogenides have outstanding chemisorption to oxygen-containing intermediates, thus exhibiting excellent OER activity.[4] Therefore, effectively combining the OER and HER electrocatalysts with high catalytic activity is expected to develop high-performance water splitting catalysts. The successful construction of heterostructures and the effective regulation of interface electronic structures are still challenging.[19-22]

Furthermore, in-depth research in recent years has shown that anion vacancy-defect engineering has been applied to significantly improve the performance of electrocatalysts by providing more active sites, increasing conductivity and enhancing stability.[23] Therefore, rational design of anion vacancy-defect engineering into the electrocatalysts can effectively achieve the goal of excellent performance. To improve the overall water splitting performance, the introduction of oxygen (O), sulfur (S) and phosphorus

DOI: 10.14102/j.cnki.0254-5861.2022-0130

(P) anion vacancy-defect into electrocatalysts have been widely reported.[24,25] Combining various progressive characterizations and DFT calculations, the contact between vacancy-defect and electrocatalysts activity has been built, which is very favorable to the design and preparation of efficient electrocatalysts with abundant vacancies to achieve the high-performance overall water splitting.[26] Thus, integrating the advantages of anion vacancies and heterostructures may increase the combining affinities to the intermediates containing oxygen and hydrogen, offer more active sites, and extremely enhance the activity of overall water splitting.

Based on the aforesaid considerations, a facile method has been used to successfully present the co-construction of sulfur vacancies and heterogeneous interface into Ni_3S_2/MoS_2 catalysts on NF. In V_S-Ni_3S_2/MoS_2 catalysts, MoS_2 nanosheets combine with Ni_3S_2 nanoparticles to form a catalytic material with multiple phase interfaces, and reducing hydrogen takes away sulfur from the catalytic surface to form abundant sulfur vacancies. The obtained V_S-Ni_3S_2/MoS_2 catalysts exhibit superior OER and HER activities, and the overpotentials for OER and HER are 180 and 71 mV at 10 mA·cm^{-2}, respectively. Furthermore, a low water splitting voltage of 1.46 V is required at 10 mA·cm^{-2} for the V_S-Ni_3S_2/MoS_2 catalysts, which is considerably lower than that of most water splitting electrocatalysts currently reported. This work offers an effective mean for the preparation of catalysts with both anion vacancies and heterostructures for achieving high-performance alkaline overall water splitting.

RESULTS AND DISCUSSION

The V_S-Ni_3S_2/MoS_2 catalysts have been synthesized by the following procedures. Firstly, the $NiMo_6$ precursor was prepared by an oil bath method,[27] and the FT-IR spectrum, XRD, and XPS of $NiMo_6$ are shown in Figure S1-3. And the NiMoS was fabricated evenly on NF via a simple hydrothermal method. Then, the NiMoS was calcined under 5% H_2/Ar at 500 °C for 2 h to form the Ni_3S_2/MoS_2 heterostructures with abundant sulfur vacancies (Figure 1a). In this procedure, hydrogen with reducibility took away sulfur from the surface of NiMoS and formed rich sulfur vacancies, making the V_S-Ni_3S_2/MoS_2 catalysts exhibit superior OER, HER, and water splitting performances.[28] Moreover, the electronegativity of metal Mo is greater than that of metal Ni, indicating that Ni is more metallic and easier to combine with S atoms, which leads to the evolution of Ni_3S_2/MoS_2 heterostructures and creates abundant sulfur vacancies at the same time.[29]

To confirm the phases and crystallinity of catalysts, the structures of these obtained electrocatalysts are comprehensively measured by Power X-ray diffraction (XRD). For V_S-Ni_3S_2/MoS_2 catalysts, the observed diffraction peaks (black line) of 21.8°, 31.1°, 49.7°, 50.1°, 55.1°, and 55.3° can be indexed to the (101), (110), (113), (211), (122), and (300) planes of the Ni_3S_2, respectively (JCPDS Card No. 44-1418). And the observed diffraction peak of 14.5° is attributed to the (003) plane of MoS_2 (JCPDS Card No. 86-2308) (Figure 1b).[30] However, the crystallinity of MoS_2 is poor before annealing at 500 °C under 5% H_2/Ar, which may be due to the fact that more hexavalent Mo (VI) is reduced to tetravalent Mo (IV) in a reducing atmosphere (Figure S4a-b). Scanning electron microscopy (SEM) image of V_S-Ni_3S_2/MoS_2

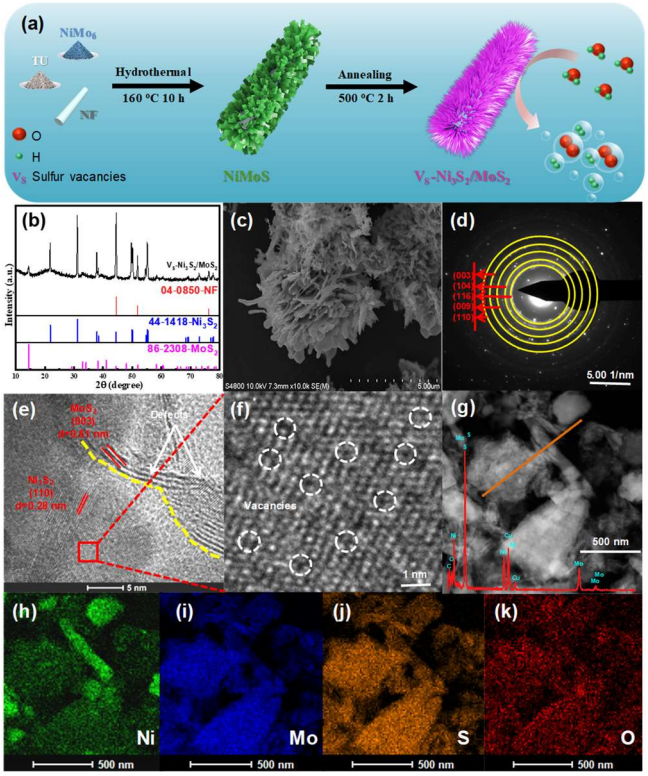

Figure 1. (a) Synthesis process for the V_S-Ni_3S_2/MoS_2 catalysts; (b) XRD patterns of the V_S-Ni_3S_2/MoS_2 catalysts; (c) SEM image of V_S-Ni_3S_2/MoS_2; (d) SAED pattern; (e,f) HRTEM images; (g) HAADF-STEM (inset shows the EDX spectra); (h-k) Element mapping results of the V_S-Ni_3S_2/MoS_2 catalysts.

catalysts has been provided in Figure 1c. The catalysts show sheet stacking morphology. The structure is further studied by the high-resolution transmission electron microscopy (HR-TEM) and selected area electron diffraction (SAED). In Figure 1e, the (110) plane of Ni_3S_2 can be clearly found with the lattice fringe spacing of 0.28 nm, and the distance of 0.61 nm can be indexed to the (003) plane of MoS_2. The results manifest that the catalysts are composed by Ni_3S_2 and MoS_2, and the heterogeneous structures are synthesized successfully.[30,31] This conclusion can be further verified by the SAED pattern (Figure 1d), exhibiting unambiguous (104) and (110) planes of Ni_3S_2 and (003), (009), and (116) planes of MoS_2. Furthermore, a lot of distortions and discrete crystal edges can be found, demonstrating abundant vacancy-defect structures had been developed (Figure 1e-f).[26,32,33] The line scanning profiles recorded have been shown in Figure 1g and S6. And the energy-dispersive X-ray spectroscopy (EDX) results reveal that all the elements are evenly distributed in the V_S-Ni_3S_2/MoS_2 catalysts (Figure 1h-k).

In order to analyze the surface components of the catalysts, X-ray photoelectron spectroscopy (XPS) of the obtained catalysts had been performed. For NiMoS and V_S-Ni_3S_2/MoS_2 catalysts, Ni 2p (4.19%), Mo 3d (6.55%), and S 2p (8.44%) regions are shown in Figure 2(a-c). Besides, the XPS spectra of C 1s (43.71%), N 1s (19.08%), and O 1s (18.02%) are shown in Figure S7(b-d). In the Ni 2p region, the peaks observed at 852.9 and 870.2 eV corre-

DOI: 10.14102/j.cnki.0254-5861.2022-0130

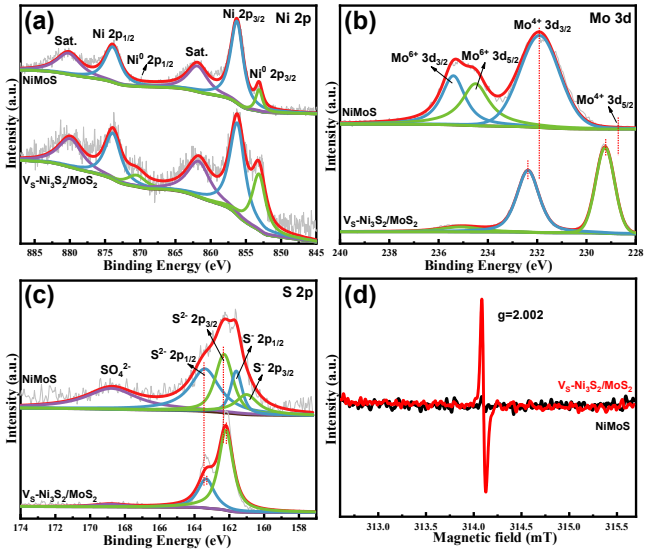

Figure 2. XPS spectra of the NiMoS and V_S-Ni_3S_2/MoS_2 catalysts: (a) Ni 2p, (b) Mo 3d, and (c) S 2p; (d) EPR spectra of the hybrid catalysts.

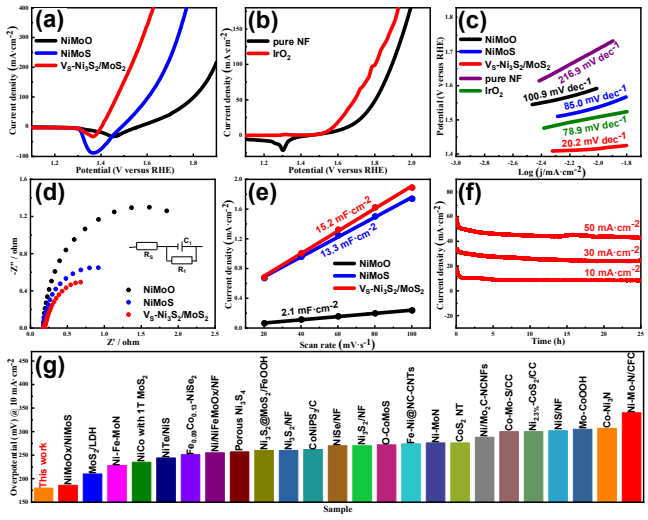

Figure 3. (a,b) OER polarization curves; (c) Tafel slopes; (d) Nyquist plots measured for various catalysts; (e) Plots showing the extraction of the C_{dl} for various catalysts; (f) The chronopotentiometric durability test of the catalysts; (g) OER overpotentials of the V_S-Ni_3S_2/MoS_2 catalysts and the reported electrocatalysts for comparison.

sponding to the typical peaks of Ni^0 due to the NF and the Ni $2p_{3/2}$ and Ni $2p_{1/2}$ typical peaks of the Ni-S bond can be also found at 855.9 and 873.6 eV.[34] In Figure 2b, the Mo 3d XPS spectra show that the $3d_{5/2}$ of Mo^{4+} and Mo^{6+} for NiMoS catalysts are observed at 228.7 and 234.5 eV, and the $3d_{3/2}$ of Mo^{4+} and Mo^{6+} are also observed at 231.9 and 235.4 eV, respectively.[35] However, the binding energy of Mo^{4+} and Mo^{6+} in V_S-Ni_3S_2/MoS_2 is higher shifted about 0.4 and 0.5 eV in comparison with that in NiMoS, which suggests the existence of strong electronic interactions between MoS_2 and Ni_3S_2.[30,36] These results further indicate that the Ni_3S_2/MoS_2 heterostructures have been synthesized. A large amount of Mo^{6+} is reduced to Mo^{4+} by hydrogen, indicating the formation of MoS_2.[35] This result is consistent with XRD. In the S 2p spectrum, a peak appears at 168.8 eV corresponding to the SO_4^{2-} characteristic peak, which may be caused by the unavoidable oxidation of surface NiMoS in air.[37] And some peaks are observed at 161.0, 161.6, 162.3 and 163.4 eV, corresponding to the S^- $2p_{3/2}$, S^- $2p_{1/2}$, S^{2-} $2p_{3/2}$ and S^{2-} $2p_{1/2}$ characteristic peaks of M-S bond for NiMoS catalysts.[38] However, for V_S-Ni_3S_2/MoS_2, the S^{2-} $2p_{3/2}$ and S^{2-} $2p_{1/2}$ characteristic peaks become stronger and move to lower binding energies of 162.1 and 163.2 eV compared to those of NiMoS in Figure 2c, manifesting the successful introduction of sulfur vacancies in the V_S-Ni_3S_2/MoS_2 catalysts.[35,38-40] Also, in order to study the sulfur vacancies, the catalysts are investigated by electron paramagnetic resonance (EPR). As found from Figure 2d, a vibration band with a g factor of 2.002 can be attributed to sulfur vacancies.[15,41] Interestingly, the EPR results show almost no vacancies or defects in NiMoS. After being reduced by hydrogen, the vacancy signal intensity of V_S-Ni_3S_2/MoS_2 catalysts increased significantly, indicating that a large amount of S vacancy has been successfully introduced into the V_S-Ni_3S_2/MoS_2 catalysts, which may greatly improve its catalytic activity.[32,33]

In order to study the effect of S vacancies and heterogeneous interface on the OER and HER properties of V_S-Ni_3S_2/MoS_2 catalysts, the electrochemical tests are implemented in 1.0 M KOH solution. The OER and HER activities of V_S-Ni_3S_2/MoS_2 catalysts are estimated by the LSV curves. The OER test was carried out at the reverse voltage from 1 to 0 V, due to the oxidation peak of NF. Significantly, the V_S-Ni_3S_2/MoS_2 catalysts exhibit excellent OER activity, and the overpotential is 180 mV at 10 $mA{\cdot}cm^{-2}$, which is much lower than those of NiMoS (274 mV), NiMoO (369 mV), pure NF (409 mV), and IrO_2 (346 mV), respectively (Figure 3a-b). Tafel slope formed by polarization curves is shown in Figure 3c to determine the reaction kinetics.[28] The results show that the introduction of S vacancies and heterogeneous interface could immensely reduce the Tafel slope from 85.0 $mV{\cdot}dec^{-1}$ (NiMoS) to 20.2 $mV{\cdot}dec^{-1}$ (V_S-Ni_3S_2/MoS_2). The Tafel slope of V_S-Ni_3S_2/MoS_2 is also much lower than that of the other catalysts, including NiMoO (100.9 $mV{\cdot}dec^{-1}$), pure NF (216.9 $mV{\cdot}dec^{-1}$), and IrO_2 (78.9 $mV{\cdot}dec^{-1}$). The electrochemical impedance spectroscopy (EIS) of the catalysts indicates the smallest semicircle for V_S-Ni_3S_2/MoS_2, which manifests low charge transfer resistance (Rct) at the electrode-electrolyte interface (Figure 3d). Besides, the electrochemically active surface area (ECSA) is also tested to evaluate the electrochemical activity by double-layer capacitance (C_{dl}) as originated from the cyclic voltammetry (CV) (Figure S9). The calculated C_{dl} values of NiMoO, NiMoS, and V_S-Ni_3S_2/MoS_2 are 2.1, 13.3, and 15.2 $mF{\cdot}cm^{-2}$, respectively (Figure 3e), indicating the co-construction of sulfur vacancies and heterogeneous interface into V_S-Ni_3S_2/ MoS_2 catalysts can provide more catalytic active sites, thus leading to the optimal electrochemical activity. The electrochemical stability of V_S-Ni_3S_2/MoS_2 catalysts during OER process is further explored by long-time LSV test at 10 $mV{\cdot}s^{-1}$ (Figure 3f). The chronoamperometric curves show that the current density remains stable for 24 h with almost no loss, indicating the excellent stability of V_S-Ni_3S_2/MoS_2 catalysts. In addition, the

Chin. J. Struct. Chem. **2022**, 41, 2208037-2208043
DOI: 10.14102/j.cnki.0254-5861.2022-0130

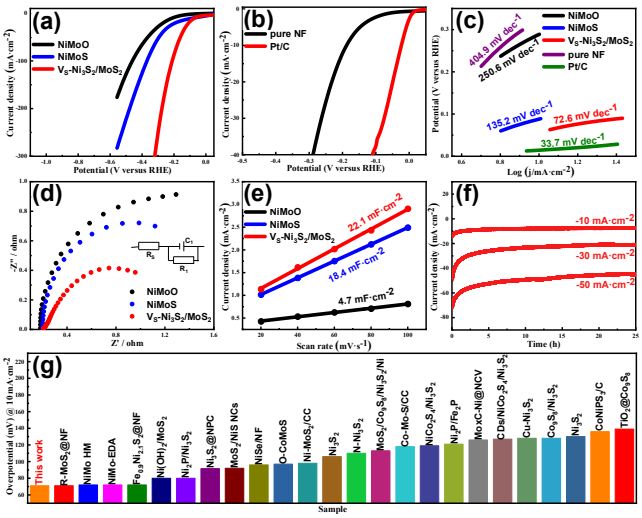

Figure 4. (a,b) HER polarization curves; (c) Tafel slopes; (d) Nyquist plots measured for various catalysts; (e) Plots showing the extraction of the C_{dl} for various catalysts; (f) Chronopotentiometric durability test of the catalysts; (g) HER overpotentials of the V_S-Ni_3S_2/MoS_2 catalysts and the reported electrocatalysts for comparison.

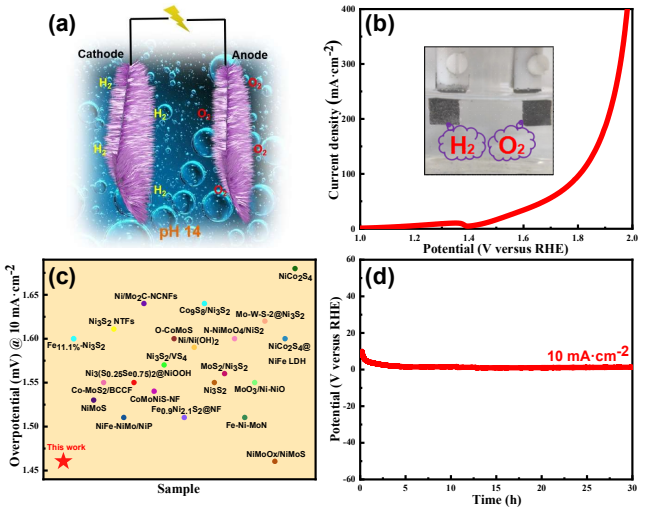

Figure 5. (a) Schematic diagram of the overall water splitting; (b) LSV curves (inset shows the photograph during overall water splitting); (c) The electrochemical overall water splitting performance of the V_S-Ni_3S_2/MoS_2 catalysts and the reported bifunctional electrocatalysts for comparison; (d) Chronopotentiometric durability test of V_S-Ni_3S_2/MoS_2.

OER catalytic activity of V_S-Ni_3S_2/MoS_2 is comparable to those of the reported electrocatalysts in alkaline media (Figure 3g and Table S2).

Meanwhile, the V_S-Ni_3S_2/MoS_2 catalysts exhibit excellent HER activity with the overpotential of 71 mV at 10 mA·cm^{-2}, much lower than those of NiMoS (80 mV), NiMoO (210 mV) and pure NF (188 mV), but not Pt/C (20 wt.%) (24.4 mV), respectively (Figure 4a-b). And the Tafel slope of V_S-Ni_3S_2/MoS_2 catalysts (72.6 mV·dec^{-1}) is also lower than that of NiMoS (135.2 mV·dec^{-1}), NiMoO (250.6 mV·dec^{-1}) and pure NF (404.9 mV·dec^{-1}) in Figure 4c. The above results indicate the co-construction of sulfur vacancies and heterogeneous interface can significantly enhance the HER property. The Nyquist plot indicates that the V_S-Ni_3S_2/MoS_2 catalysts has the lowest EIS value (Figure 4d). The ECSA is also characterized by the C_{dl} in Figure S13. The calculated C_{dl} values of NiMoO, NiMoS, and V_S-Ni_3S_2/MoS_2 are 4.7, 18.4, and 22.1 mF·cm^{-2}, respectively (Figure 4e), which shows better HER activity for V_S-Ni_3S_2/MoS_2. Furthermore, the chronoamperometric curve reveals the outstanding HER stability of V_S-Ni_3S_2/MoS_2 catalysts (Figure 4f). The HER catalytic activity of V_S-Ni_3S_2/MoS_2 is comparable to those of the reported electrocatalysts in KOH solution (Figure 4g and Table S3).

Owing to the excellent OER and HER electrochemical activities, a water splitting device by using V_S-Ni_3S_2/MoS_2 catalysts as the bifunctional electrocatalysts has been assembled and carried out in 1.0 M KOH solution (Figure 5a). A current density of 10 mA·cm^{-2} is delivered at probably 1.46 V for the electrochemical overall water splitting (Figure 5b). In addition, the V_S-Ni_3S_2/MoS_2 catalysts still show superiority to the other recently reported overall water splitting catalysts (Figure 5c and Table S4). In Figure 5d, the chronopotentiometric curve at 1.46 V (at 10 mV·s^{-1}) exhibits that the current density keeps persistent approximately up to 30 h with few degradations, further confirming the excellent stability of V_S-Ni_3S_2/MoS_2 catalysts. In addition, the Faraday efficiency is measured and calculated to evaluate the catalytic efficiency of V_S-Ni_3S_2/MoS_2 catalysts. As can be seen, the current efficiency of generating oxygen is 98.8%, and the efficiency of generating hydrogen is 98.6% in the process of overall water splitting (Figure S17).

The aforesaid experiment results show that the co-construction of sulfur vacancies and heterogeneous interface into the VS-Ni_3S_2/MoS_2 catalysts has multiple advantages:[42-44] Firstly, the formed Ni_3S_2/MoS_2 heterostructures could increase supernumerary charge transfer to strengthen the reaction kinetics benefiting from the build-in electric field effect, and the regulation of interface electronic structure is beneficial to enhance catalytic activity. Se-

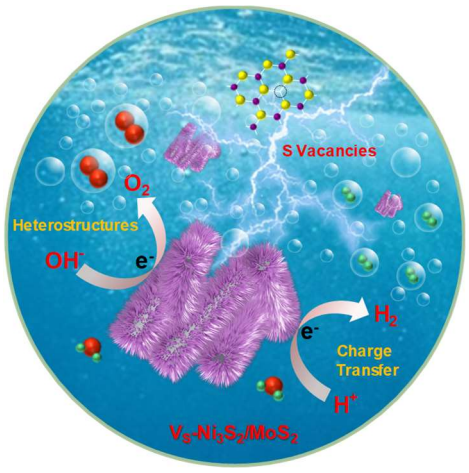

Figure 6. Schematic illustration for the catalytic mechanism of V_S-Ni_3S_2/MoS_2 catalysts.

DOI: 10.14102/j.cnki.0254-5861.2022-0130

condly, the vacancies generated in Ni_3S_2/MoS_2 catalysts can supply abundant active sites, adjust the d-band center, and enhance the catalytic activity. Finally, the synergistic effect of sulfur vacancies and heterogeneous interface can significantly reduce the adsorption free energy of intermediates, thereby enhancing catalytic performance (Figure 6).

CONCLUSION

In summary, a novel V_S-Ni_3S_2/MoS_2 heterostructure with abundant sulfur vacancies is successfully synthesized in this work. Benefited from the co-construction of sulfur vacancies and heterogeneous interface, the V_S-Ni_3S_2/MoS_2 catalysts show superior OER, HER, and overall water splitting performances. The overpotentials for OER and HER are 180 and 71 mV at 10 mA·cm^{-2}, and a low water splitting voltage of 1.46 V is required at 10 mA·cm^{-2}. The results indicate that the sulfur vacancies and heterogeneous interface in V_S-Ni_3S_2/MoS_2 can supply a large number of active sites and significantly improve the transport of electrons and ions, thus enhancing the catalytic performances. This work offers an effective mean for the preparation of catalysts with both anion vacancies and heterostructures for achieving high-performance alkaline overall water splitting.

EXPERIMENTAL

Material and Reagents. The chemicals, such as $Ni(NO_3)_2·6H_2O$, $(NH_4)_6Mo_7O_{24}·4H_2O$, CH_4N_2S (TU), and ethanol used in this work are purchased from Aladdin without further improvement purification. The washing solvents applied in the process of material synthesis are deionized water and ethanol.

Synthesis of $(NH_4)_4[Ni(II)Mo_6O_{24}H_6]·5H_2O$ ($NiMo_6$). $Ni(NO_3)_2·6H_2O$ (0.87 g, 3 mmol) in 20 mL deionized water was added into a boiling aqueous solution of $(NH_4)_6Mo_7O_{24}·4H_2O$ (5.2 g, 4.2 mmol) in 80 mL deionized water. The obtained solution was further evaporated on the steam-bath about for 10 min and cooled to room temperature to get some light blue crystals of $NiMo_6$ which were then recycled twice from deionized water to obtain a clean crystal. Finally, the sample was collected by filtration and dried at 60 °C for 10 h.

Synthesis of V_S-Ni_3S_2/MoS_2 on NF. Prior to synthesis, a 2 × 3 cm^2 of NF was respectively ultrasounded with HCl (1 M), acetone, and ethanol absolute maintaining 15 min to ensure that there is no oxide and other materials on the surface. In order to obtain a well-mixed solution, $NiMo_6$ (0.12 g, 0.1 mmol) and TU (0.2 g, 2.7 mmol) were dissolved ultrasonically in 15 mL deionized water for 20 min. Then, the mixed solution and one piece of NF (2 × 3 cm^2) were added into a 25 mL Teflon-lined stainless-steel autoclave, and reacted at 160 °C for 10 h. The resultant NiMoS was washed several times using deionized water and ethanol after naturally cooling to room temperature and dried at 60 °C for 10 h. In the second step, NiMoS was calcined at 500 °C under 5% H_2/Ar for 2 h to form V_S-Ni_3S_2/MoS_2.

Synthesis of NiMoS on NF. The preparatory processes of NiMoS is similar to that of V_S-Ni_3S_2/MoS_2. It's just that there's no the second step.

Synthesis of NiMoO on NF. The preparatory processes of NiMoO are similar to that of NiMoS, just withour TU in the hydrothermal step.

Materials Characterization. X-ray diffraction (XRD) profiles (2θ, 5-80°) were acquired on a PuXi XD3 diffractometer with Cu Kα (λ = 0.15406 nm). X-ray photoelectron spectra (XPS) were corrected using the C 1s line at 284.6 eV, and measured using an ESCALAB 250 X-ray electron spectrometer equipped with Al Kα radiation. The scanning electron microscopy (SEM) images were performed on Field Emission Scanning Electron Microscopy (FESEM, JEOL JSM-7600F). Transmission electron microscopy (TEM) and high-resolution transmission electron microscopy (HRTEM) images were recorded on a JEM-2010 transmission electron microscope system. Electron paramagnetic resonance (EPR) tests were performed using the EPRA300-9.5/12 (Bruker) electron paramagnetic resonance spectrometer.

Electrochemical Measurements. The OER, HER, and water-splitting activities of the obtained catalysts were performed on an electrochemical workstation (CHI 760E), and tested in 1.0 M KOH. A standard three-electrode system had been used, and the NF based electrodes, graphite plate (area: 0.5 × 1.0 cm^2), and Hg/Hg_2Cl_2 were used as the working, counter, and reference electrodes, respectively. The linear sweep voltammetry (LSV) polarization curves were tested with a scan rate of 5 mV·s^{-1} with the iR correction of 80%. The double-layer capacitance (C_{dl}) of the obtained samples was measured by using cyclic voltammetry (CV) with various scan rates in a non-Faradaic region. Electrochemical impedance spectroscopy (EIS) was performed in 1.0 M KOH solution at 0.4 V with an amplitude of 5 mV. The chronoamperometric durability curves (i-t) and chronopotentiometric durability curves (v-t) were measured with a constant potential to investigate the chemical stability in 1.0 M KOH solution.

ACKNOWLEDGEMENTS

This project was financially supported by the National Natural Science Foundation of China (NSFC 21666023, 21467019, 21701168), Natural Science Foundation of Inner Mongolia Autonomous Region of China (2021ZD11, 2019BS02015), Program for Young Talents of Science and Technology in Universities of Inner Mongolia Autonomous Region (NJYT-19-A01), and Postsubsidy Funds for the Inner Mongolia Key Laboratory of Chemistry and Physics of Rare Earth Materials (2021PT0003).

AUTHOR INFORMATION

Corresponding authors. Emails: qinwang@imu.edu.cn (Q. Wang) and hxue@imu.edu.cn (H. Xue)

COMPETING INTERESTS

The authors declare that they have no known competing financial interests or personal relationships that could have appeared to influence the work reported in this paper.

ADDITIONAL INFORMATION

Supplementary information is available for this paper at http://manu30.magtech.com.cn/jghx/EN/10.14102/j.cnki.0254-5861.2022-0130

DOI: 10.14102/j.cnki.0254-5861.2022-0130

For submission: https://mc03.manuscriptcentral.com/cjsc

REFERENCES

(1) Yang, J. L.; He, Y. L.; Ren, H.; Li, J. F. Boosting photocatalytic hydrogen evolution reaction using dual plasmonic antennas. *ACS Catal.* **2021**, 11, 5047-5053.

(2) Xue, Z. Z.; Meng, X. D.; Pan, J.; Wang, G. M. Luminescent thermochromism and white-light emission of a 3D $[Ag_4Br_6]$ cluster-based coordination framework with both adamantane-like node and linker. *Inorg. Chem.* **2021**, 60, 4375-4379.

(3) Mu, Y.; Wang, D.; Meng, X. D.; Xue, Z. Z. Construction of iodoargentates with diverse architectures: template syntheses, structures, and photocatalytic properties. *Cryst. Growth Des.* **2020**, 20, 1130-1138.

(4) Zang, Z. H.; Wang, X. W.; Li, X.; Lu, Z. M. Co_9S_8 nanosheet coupled Cu_2S nanorod heterostructure as efficient catalyst for overall water splitting. *ACS Appl. Mater. Interfaces* **2021**, 13, 9865-9874.

(5) Esposito, D. V.; Hunt, S. T.; Stottlemyer, A. L.; Chen, J. G. G. Low-cost hydrogen-evolution catalysts based on monolayer platinum on tungsten monocarbide substrates. *Angew. Chem. Int. Ed.* **2010**, 122, 10055-10058.

(6) Zeng, K.; Zhang, D. K. Recent progress in alkaline water electrolysis for hydrogen production and applications. *Prog. Energy Combust. Sci.* **2010**, 36, 307-326.

(7) Man, I. C.; Su, H. Y.; Calle-Vallejo, F.; Rossmeisl, J. Universality in oxygen evolution electrocatalysis on oxide surfaces. *ChemCatChem* **2011**, 3, 1159-1165.

(8) Subbaraman, R.; Tripkovic, D.; Strmcnik, D.; Markovic, N. M. Enhancing hydrogen evolution activity in water splitting by tailoring Li^+-$Ni(OH)_2$-Pt interfaces. *Science* **2011**, 334, 1256-1260.

(9) Lin, C.; Li, J. L.; Li, X. P.; Yang, S. In-situ reconstructed Ru atom array on α-MnO_2 with enhanced performance for acidic water oxidation. *Nat. Catal.* **2021**, 4, 1012-1023.

(10) Li, Z. J.; Wu, X. D.; Jiang, X.; Shen, B. B. Surface carbon layer controllable Ni_3Fe particles confined in hierarchical N-doped carbon framework boosting oxygen evolution reaction. *Adv. Powder Mater.* **2022**, 1, 100020.

(11) Lin, C.; Li, X. P.; Shinde, S. S.; Kim, D. H. Long-life rechargeable Zn air battery based on binary metal carbide armored by nitrogen-doped carbon. *ACS Appl. Energy Mater.* **2019**, 2, 1747-1755.

(12) Wang, J. H.; Cui, W.; Liu, Q.; Sun, X. P. Recent progress in cobalt-based heterogeneous catalysts for electrochemical water splitting. *Adv. Mater.* **2016**, 28, 215-230.

(13) Yan, Y.; Xia, B. Y.; Xu, Z. C.; Wang, X. Recent development of molybdenum sulfides as advanced electrocatalysts for hydrogen evolution reaction. *ACS Catal.* **2014**, 4, 1693-1705.

(14) Jaramillo, T. F.; Jorgensen, K. P.; Bonde, J.; Chorkendorff, I. Identification of active edge sites for electrochemical H_2 evolution from MoS_2 nanocatalysts. *Science* **2007**, 317, 100-102.

(15) Sun, J.; Guo, N. K.; Shao, Z. Y.; Wang, Q. A facile strategy to construct amorphous spinel-based electrocatalysts with massive oxygen vacancies using ionic liquid dopant. *Adv. Energy Mater.* **2018**, 8, 1800980.

(16) Hao, S. Y.; Chen, L. C.; Yu, C. L.; Zhang, X. W. NiCoMo hydroxide nanosheet arrays synthesized via chloride corrosion for overall water splitting. *ACS Energy Lett.* **2019**, 4, 952-959.

(17) Li, P. S.; Duan, X. X.; Kuang, Y.; Sun, X. M. Tuning electronic structure of NiFe layered double hydroxides with vanadium doping toward high efficient electrocatalytic water oxidation. *Adv. Energy Mater.* **2018**, 8, 1703341.

(18) Doan, T. L. L.; Tran, D. T.; Nguyen, D. C.; Lee, J. H. Rational engineering CoxOy nanosheets via phosphorous and sulfur dual-coupling for enhancing water splitting and Zn-air battery. *Adv. Funct. Mater.* **2020**, 31, 2007822.

(19) Wu, J.; Xie, Y.; Du, S. C.; Fu, H. G. Heterophase engineering of SnO_2/Sn_3O_4 drives enhanced carbon dioxide electrocatalytic reduction to formic acid. *Sci. China Mater.* **2020**, 63, 2314-2324.

(20) Lin, K.; Xiao, F.; Xie, Y.; Fu, H. G. Surface domain heterojunction on rutile TiO_2 for high-efficient photocatalytic hydrogen evolution. *Nanoscale Horiz.* **2020**, 5, 1596-1602.

(21) Tong, M. M.; Sun, F. F.; Xie, Y.; Fu, H. G. Operando cooperated catalytic mechanism of atomically dispersed Cu-N_4 and Zn-N_4 for promoting oxygen reduction reaction. *Angew. Chem. Int. Ed.* **2021**, 60, 2-10.

(22) Wu, A. P.; Gu, Y.; Yang, B. R.; Fu, H. G. Porous cobalt/tungsten nitride polyhedra as efficient bifunctional electrocatalysts for overall water splitting. *J. Mater. Chem. A* **2020**, 8, 22938-22946.

(23) Tang, Y. Q.; Shen, H. M.; Cheng, J. Q.; Zou, R. Q. Fabrication of oxygen-vacancy abundant NiMn-layered double hydroxides for ultrahigh capacity supercapacitors. *Adv. Funct. Mater.* **2020**, 30, 1908223.

(24) Xiao, Z. H.; Huang, Y. C.; Dong, C. L.; Wang, S. Y. Operando identification of the dynamic behavior of oxygen vacancy-rich Co_3O_4 for oxygen evolution reaction. *J. Am. Chem. Soc.* **2020**, 142, 12087-12095.

(25) Liang, Z. Z.; Huang, Z. H.; Yuan, H. Y.; Cao, R. Quasi-single-crystalline CoO hexagrams with abundant defects for highly efficient electrocatalytic water oxidation. *Chem. Sci.* **2018**, 9, 6961-6968.

(26) Gao, Y.; Liu, C. B.; Zhou, W.; Zhang, B. Anion vacancy engineering in electrocatalytic water splitting. *ChemNanoMat* **2020**, 6, 1-9.

(27) Tang, Y. J.; Zhang, A. M.; Zhu, H. J.; Lan, Y. Q. Polyoxometalate precursors for precisely controlled synthesis of bimetallic sulfide heterostructure through nucleation-doping competition. *Nanoscale* **2018**, 10, 8404-8412.

(28) Zhu, Q.; Chen, W. Z.; Cheng, H.; Pan, H. WS_2 nanosheets with highly-enhanced electrochemical activity by facile control of sulfur vacancies. *ChemCatChem* **2019**, 11, 2667-2675.

(29) Li, Y.; Qian, J.; Zhang, M. H.; Wu, C. Co-construction of sulfur vacancies and heterojunctions in tungsten disulfide to induce fast electronic/ionic diffusion kinetics for sodium-ion batteries. *Adv. Mater.* **2020**, 32, 2005802.

(30) Zhang, J.; Wang, T.; Pohl, D.; Feng, X. L. Interface engineering of MoS_2/Ni_3S_2 heterostructures for highly enhanced electrochemical overall-water-splitting activity. *Angew. Chem. Int. Ed.* **2016**, 128, 6814-6819.

(31) Wu, A. P.; Gu, Y.; Xie, Y.; Fu, H. G. Effective electrocatalytic hydrogen evolution in neutral medium based on 2D MoP/MoS_2 heterostructure nanosheets. *ACS Appl. Mater. Interfaces* **2019**, 11, 25986-25995.

(32) Cai, L.; He, J. F.; Liu, Q. H.; Sun, Z. H. Vacancy-induced ferromagnetism of MoS_2 nanosheets. *J. Am. Chem. Soc.* **2015**, 137, 2622-2627.

(33) Ling, C. C.; Liu, X. F.; Li, M. Q.; Zhang, L. Z. Sulphur vacancy derived anaerobic hydroxyl radical generation at the pyrite-water interface: pollutants removal and pyrite self-oxidation behavior. *Appl. Catal. B-Environ.* **2021**, 290, 120051.

(34) Zhang, B.; Xiao, C. H.; Xie, S. M.; Tang, Y. H. Iron-nickel nitride nanostructures in situ grown on surface-redox-etching nickel foam: efficient and ultrasustainable electrocatalysts for overall water splitting. *Chem. Mater.* **2016**, 28, 6934-6941.

(35) Zhai, P. L.; Zhang, Y. X.; Wu, Y. Z.; Hou, J. G. Engineering active sites

DOI: 10.14102/j.cnki.0254-5861.2022-0130

on hierarchical transition bimetal oxides/sulfifides heterostructure array enabling robust overall water splitting. *Nat. Commun.* **2020**, 11, 5462.

(36) Fei, B.; Chen, Z. L.; Liu, J. X.; Wu, R. B. Ultrathinning nickel sulfide with modulated electron density for efficient water splitting. *Adv. Energy Mater.* **2020**, 10, 2001963.

(37) Feng, X. T.; Jiao, Q. Z.; Dai, Z.; Li, A. Revealing the effect of interfacial electron transfer in heterostructured Co_9S_8@NiFe LDH for enhanced electrocatalytic oxygen evolution. *J. Mater. Chem. A* **2021**, 9, 12244-12254.

(38) Zhang, J. Y.; Xiao, W.; Gao, D. Q.; Ding, J. Activating and optimizing activity of CoS_2 for hydrogen evolution reaction through the synergic effect of N dopants and S vacancies. *ACS Energy Lett.* **2017**, 2, 1022-1028.

(39) Dong, X.; Jiao, Y. Q.; Yang, G. C.; Fu, H. G. One-dimensional Co_9S_8-V_3S_4 heterojunctions as bifunctional electrocatalysts for highly efficient overall water splitting. *Sci. China Mater.* **2021**, 64, 1396-1407.

(40) Wang, H.; Li, Z. J.; Li, Y.; Hou, Y. An exfoliated iron phosphorus trisulfide nanosheet with rich sulfur vacancy for efficient dinitrogen fixation and Zn-N_2 battery. *Nano Energy* **2021**, 81, 105613.

(41) Shao, Z. Y.; Liu, R. B.; Xue, H.; Wang, Q. Regulating the electronic structure of ultrathin Ni-based chalcogenide nanosheets through iron modification towards high electrocatalytic activities. *Chem. Eng. J.* **2021**, 416, 129098.

(42) Li, S. L.; Ma, R. G.; Hu, J. C.; Li, Z. C. Coordination environment tuning of nickel sites by oxyanions to optimize methanol electro-oxidation activity. *Nat. Commun.* **2022**, 13, 2916.

(43) Wang, X. L.; Ma, R. G.; Wang, M. M.; Wang, J. Hollow MoS_2/Co nanopillars with boosted Li-ion diffusion rate and long-term cycling stability. *Chem. Commun.* **2021**, 57, 11521-11524.

(44) Zhu, L.; Liao, Y. X.; Jia, Y. B.; Zhang, X. Solid-solution hexagonal $Ni_{0.5}Co_{0.5}Se$ nanoflakes toward boosted oxygen evolution reaction. *Chem. Commun.* **2020**, 56, 13113-13116.

Received: May 20, 2022
Accepted: June 2, 2022
Published online: July 11, 2022
Published: July 25, 2022

DOI: 10.14102/j.cnki.0254-5861.2022-0130